Int. J. Heat Mass Transfer. Vol. 31, No. 3, pp. 461–477, 1988
Printed in Great Britain

0017–9310/88 $3.00 + 0.00
Pergamon Press plc

Models and solutions for isothermal and non-isothermal evaporation from a partially filled tube

G. A. NUNEZ and E. M. SPARROW

Department of Mechanical Engineering, University of Minnesota, Minneapolis, MN 55455, U.S.A.

(*Received* 20 *May* 1987 *and in final form* 3 *August* 1987)

Abstract—Evaporation from a liquid pool which partially fills a circular tube into an otherwise quiescent ambient has been investigated by a succession of models and accompanying numerical solutions. The modeling included consideration of: (a) evaporation occurring under both isothermal and non-isothermal conditions as related to the absence or presence of depression of the temperature at the liquid surface, (b) interactions between the velocity, mass fraction, and temperature fields in the gas–vapor space in the tube and in the ambient, (c) natural convection in the gas–vapor space, (d) radiative interchange in the gas–vapor space, (e) natural convection in the liquid pool, and (f) conduction in the insulation surrounding the tube, in the tube wall, and in the liner between the tube and the insulation. By using a special set of closure conditions at the open top of the tube, it was found that evaporation rates (i.e. Sherwood numbers) of acceptable accuracy can be obtained without having to extend the numerical solutions into the ambient. Another key finding was that the depression of the temperature at the liquid surface decreased the Sherwood number. When radiative transfer in the gas–liquid space was activated, the temperature depression diminished and the Sherwood number markedly increased. Natural convection in the liquid pool also acted to lessen the temperature depression and to increase the Sherwood number.

INTRODUCTION

THIS PAPER is concerned with the formulation and numerical implementation of analytical models for the evaporation of a liquid from a partially filled cylindrical tube. The tube is vertical, and its upper end is open to a fluid environment consisting of a binary mixture of a gas and the vapor of the evaporating liquid. Aside from effects associated with the presence of the tube (to be explored here), the environment is quiescent and of uniform temperature and uniform species concentration. Although the formulation is general, the specific focus of the work is on the evaporation of water into air which contains water vapor.

The modeling/computational effort to be described here was taken from a larger work [1] which also included experiments. The experiments will not be reported here because the description of the modeling and computational work already constitutes a paper of substantial length. However, the course of the modeling and computations was guided by the need to provide predictions for comparison with the experimental data. Therefore, frequent reference will be made to the experiments and to the conditions under which they were performed.

If the partial pressure of the vapor in the ambient is lower than the vapor pressure at the surface of the liquid pool which occupies the lower portion of the tube, evaporation will occur at the surface. In steady-state operation, energy must be supplied to the surface to satisfy the latent heat requirements of the evaporation process. In general, the energy may be delivered to the surface through the gaseous mixture or through the liquid pool. The energy delivered through the gaseous mixture is drawn from the ambient at the top of the tube, while that delivered through the liquid flows from the ambient to the tube wall and then into the liquid.

If the tube is uninsulated and made of high conductivity material, then the liquid temperature is virtually identical to that of the ambient. The gas–vapor mixture also takes on the ambient temperature. Thus, the entire system is virtually isothermal. This is one of the cases to be analyzed here and which was investigated experimentally in ref. [1].

When the tube is made from a low conductivity material and is well insulated, the aforementioned latent heat requirements for evaporation are supplied in significant part by energy passing from the ambient through the gas–vapor mixture to the liquid surface. Because of the finite thermal resistance of this heat flow path, the temperature of the surface must take on a value below that of the ambient. The extent of this temperature depression depends on the quality of the insulation at the tube wall as well as on the thermal resistance of the path through the gaseous mixture.

The situation described in the preceding paragraph will be termed non-isothermal evaporation. It is the second general case to be treated here and studied experimentally in ref. [1].

All of the analytical and experimental work encompassed by the present investigation deals with the evaporation of a vapor the molecular weight of which is lower than that of the gas (e.g. water vapor evaporating into air). For this condition and for the aforementioned case of isothermal evaporation, the density

NOMENCLATURE

c_p	specific heat
D	mass diffusion coefficient
d	inner diameter of tube
F	angle factor
g	acceleration of gravity
h_{fg}	latent heat of evaporation
K	mass transfer coefficient, equation (29)
k	thermal conductivity
L	distance between liquid surface and top of tube
M	molecular weight
$\dot{M}$	overall rate of evaporation
$\dot{m}$	local rate of evaporation
p	pressure
q_{rad}	net rate of radiative transfer per unit area
R	inner radius of tube
Ra	Rayleigh number, equation (26)
r	radial coordinate
Sc	Schmidt number
Sh	Sherwood number, Kd/D
T	temperature
T_{int}	temperature at interface between subdomains
T_s	liquid surface temperature
T_∞	ambient temperature
u	axial velocity component
v	radial velocity component
W_1	mass fraction of vapor
W_{1s}	value of W_1 at liquid surface
$W_{1\infty}$	value of W_1 in ambient
x	axial coordinate.

Greek symbols

μ	viscosity
ν	kinematic viscosity
ρ	density
σ	Stefan–Boltzmann constant
ϕ_∞	relative humidity of vapor in ambient.

Subscripts

ins	insulation
s	liquid surface
1	vapor
2	gas
∞	ambient.

Superscripts

*	reference state for properties in gas–vapor space (subdomain II)
**	reference state for properties in subdomain I.

of the gas–vapor mixture will increase in the upward direction from the liquid surface to the top of the tube. This situation is unstable and will give rise to natural convection motions.

For the case of non-isothermal evaporation, the decrease of the temperature of the gas–vapor mixture in the downward vertical direction opposes the establishment of the species-related upward increase of the mixture density. The resulting shape of the density variation depends on the extent of the temperature depression. Natural convection may still occur in non-isothermal evaporation, but its vigor will be diminished relative to that for the isothermal evaporation case.

From the foregoing discussion, the inclusion of natural convection is seen to be an essential feature of the modeling. Another issue which has to be addressed in both the isothermal and non-isothermal cases is the effect of the transport processes in the tube on the ambient. When natural convection occurs in the tube, fluid will stream between the ambient and the tube, with inflow occurring over part of the tube opening and outflow occurring over the other part.

The fluid outflow from the tube to the ambient possesses vapor and temperature levels which cause departures from the otherwise uniform ambient species concentration and temperature (temperature effects are confined to the case of non-isothermal evaporation). The size of the ambient region affected by these induced nonuniformities is also unknown. Inclusion of the ambient in a numerical simulation of the in-tube evaporation problem demands significant computational resources.

There are a number of other modeling issues that have to be considered specifically for the non-isothermal evaporation problem. The simplest of these is heat conduction in the insulation layer which surrounds the tube and in the tube wall itself. A more complex issue is the heat transfer and fluid flow in the liquid pool, with the fluid motions being induced by buoyancy brought about by temperature differences. Finally, there is the somewhat subtle issue of radiative transfer between the water surface, the tube wall, and the ambient.

The foregoing discussion has served to outline the participating physical processes. Now, attention will be turned to setting forth the modeling of these processes.

The first phase of the modeling work will be entitled: The Simplest Isothermal and Non-isothermal Models. Here, consideration is confined to the gas–vapor mixture which fills the space between the liquid surface and the open top of the tube. For this region, numerical solutions were carried out for the governing differential equations expressing conservation of momentum, mass of the mixture, mass of

the vapor, and energy (for the non-isothermal case). For the isothermal case, the only noteworthy approximation is the neglect of the interaction between the tube and the ambient. Thus, for this case, the model can be regarded as a possible source of valid results for the rate of evaporation.

Non-isothermality is activated by parametrically prescribing the temperature of the surface of the liquid pool, while neglecting all of the processes discussed in an earlier paragraph. This neglect constitutes a severe oversimplification. Yet, the results from this model will be useful in demonstrating certain trends and, more importantly, as a basis for comparisons with the next level of modeling.

The next phase of the modeling is entitled: Assessment of the Role of the Ambient. The modeling involves the coupling of the aforementioned simplest models, which were restricted to the gas–vapor region of the tube, with a cylindrical region in the ambient within which the tube-related deviations from uniformity are assumed to be confined. Parametric variations were made in the size of the cylindrical region to properly account for the tube–ambient interactions. The governing conservation equations were solved numerically for the two regions of the solution domain.

For the isothermal case, this model and its numerical results mark the terminal point of the modeling, since there are no further refinements to be made. However, for the non-isothermal case, this is only a way station, but one which yields an important finding. Specifically, comparison of the results from the simplest model with those from the ambient-including model show deviations in the 5% range for the rate of evaporation. This finding provides license for the neglect of the ambient in the subsequent in-depth modeling of the non-isothermal case, where all of the many processes that were discussed earlier will be taken into account.

The final phase of the modeling bears the title: In-depth Modeling of the Non-isothermal Case. All the models considered in this phase of the work include mass, heat, and momentum transfer in the gas–vapor mixture which occupies the space between the liquid surface and the top of the tube. Model NI 1 (NI ~ non-isothermal) adds heat conduction in the insulation surrounding the tube and in the liquid pool. To this, model NI 2 adds radiative transfer between the liquid surface, the tube wall, and the ambient. Natural convection in the liquid pool is added in model NI 3. Finally, in model NI 4, heat conduction in the tube wall is added, plus, for fidelity with the experimental setup, heat conduction in a liner situated between the tube and the surrounding insulation. Numerical solutions were obtained for each of these complex systems.

The menu of this paper is now complete, and attention will be turned to the literature. Aside from an earlier work by the authors [2], to be discussed shortly, it appears that all prior studies of evaporation from a partially filled tube were restricted to diffusion-driven transport in the gas–vapor mixture situated between the liquid surface and the tube opening. No consideration was given to features such as natural convection and radiation, participation of the ambient, heat transfer and fluid flow in the liquid pool, and conduction in the insulation and tube wall.

The isothermal version of the diffusion-driven evaporation problem is the classical Stefan diffusion problem, which is widely reported in the literature (e.g. refs. [3–6]). The results of the Stefan problem have been used as the basis of an experimental method for determining the mass diffusion coefficient [7, 8]. The problem of non-isothermal diffusion-driven evaporation was treated in ref. [9], where it was assumed that the latent heat requirement was totally supplied by energy passing from the ambient through the gas–vapor mixture to the liquid surface.

In ref. [2], the present authors dealt with the isothermal version of what has been designated here as the simplest model. That work will be repeated here for more realistic operating parameters.

THE SIMPLEST ISOTHERMAL AND NON-ISOTHERMAL MODELS

The solution domain for these models is the portion of the tube between the surface of the liquid and the open top. This space is filled with the gas–vapor mixture. The tube is of radius R, and the distance between the liquid surface and the top of the tube is L. The coordinates to be used in the analysis are x, r cylindrical coordinates centered at the mid-point of the liquid surface, with x pointing vertically upward. In terms of these coordinates, the solution domain is defined by $0 \leqslant r \leqslant R$, $0 \leqslant x \leqslant L$.

In the analysis, the vapor will be denoted by subscript 1, while subscript 2 will be used to denote the gas. It will be assumed that the liquid surface is impermeable to the gas.

The isothermal case

In this case, the temperature is uniform throughout the solution domain and equal to the ambient temperature T_∞. The vapor pressure in the ambient is maintained at a value below the vapor pressure at the liquid surface (equal to the saturation pressure corresponding to T_∞), so that evaporation occurs.

The fluid flow and mass transfer are governed by four conservation equations:

conservation of x-momentum

$$\rho^*[u(\partial u/\partial x)+v(\partial u/\partial r)] = -\partial p/\partial x+\mu^*\nabla^2 u-\rho g; \tag{1}$$

conservation of r-momentum

$$\rho^*[u(\partial v/\partial x)+v(\partial v/\partial r)] = -\partial p/\partial r+\mu^*(\nabla^2 v-v/r^2); \tag{2}$$

mass conservation for the mixture

$$\partial u/\partial x+\partial v/\partial r+v/r=0; \tag{3}$$

mass conservation for species 1

$$u(\partial W_1/\partial x)+v(\partial W_1/\partial r)=D^*\nabla^2 W_1 \tag{4}$$

where W_1 is the mass fraction of the vapor.

In these equations, ρ^*, μ^*, and D^* represent constant property values. In particular

$$\rho^*=(\rho_\infty+\rho_s)/2 \tag{5}$$

while μ^* is the viscosity of the gas evaluated at the (uniform) temperature T_∞, and

$$D^*=\mu^*/\rho^* Sc \tag{6}$$

in which the Schmidt number Sc is a constant. In equation (5), ρ_∞ and ρ_s respectively denote the densities of the gas–vapor mixture in the ambient (subscript ∞) and at the liquid surface (subscript s).

The key feature of these equations is the variation of the mixture density ρ which appears in the body force term of equation (1). Note that in the present formulation, buoyancy will emerge automatically as a consequence of the density variations. This is in contrast to the conventional practice whereby a buoyancy term is created by adding and subtracting $\rho_{ref}g$ to the right-hand side of equation (1).

The density is represented by the perfect gas law

$$\rho=(p/\bar{R}T)M \tag{7}$$

where $\bar{R}$ is the universal gas constant, and M is the molecular weight. In terms of the molecular weights M_1 and M_2 of the components and of the *local* mass fraction W_1 of the vapor, M is given by

$$M=M_1M_2/[W_1M_2+(1-W_1)M_1]. \tag{8}$$

Since W_1 varies throughout the solution domain, so do M and ρ.

Attention may now be turned to the boundary conditions. At the liquid surface ($x=0$)

$$v=0 \quad \text{and} \quad W_1=W_{1s}. \tag{9}$$

Note that W_{1s} was not specified as such but rather was determined from other prescribed conditions as follows. Since $T_s=T_\infty$ in the problem under consideration and since the liquid surface is a saturation state, then $p_{1s}=p_{1,sat}$ corresponding to T_∞. Also, since the total pressure p is virtually constant, then $p_{2s}=p-p_{1s}$ can be found, from which ρ_{2s} follows from the perfect gas law. Then

$$W_{1s}=\rho_{1s}/(\rho_{1s}+\rho_{2s}) \tag{10}$$

where ρ_{1s} is the saturation density of the vapor at temperature $T_s=T_\infty$.

The velocity u perpendicular to the liquid surface is not zero because the surface is impermeable to the gas. There is a diffusive flow of the gas toward the surface because the partial pressure of the gas decreases with decreasing x. This diffusive flow must be balanced by a convective flow away from the surface (i.e. in the positive x-direction) in order that the *net* flow of the gas be zero at the surface. The velocity associated with this convective flow is derived in standard textbooks (e.g. equation (5-23) in ref. [6]) as

$$u=-[D/(1-W_{1s})](\partial W_1/\partial x)_{x=0} \tag{11}$$

where D will be evaluated as D^*.

The boundary conditions at the open top of the tube ($x=L$) were selected to enable the in-tube solution to be obtained without having to deal with tube–ambient interactions. The selected velocity conditions are

$$v=0, \quad \partial u/\partial x=0. \tag{12}$$

These closure conditions do not impose prejudicial constraints on the velocity field provided that the finite-difference grid used in the numerical solutions is closely packed in the region adjacent to the top of the tube.

With regard to the mass fraction, fluid flowing from the ambient into the tube will carry the ambient vapor mass fraction $W_{1\infty}$, assumed, at present, to be unaffected by the presence of the tube. On the other hand, fluid that exits the tube will carry mass fractions greater than $W_{1\infty}$ which, however, are unknown. These observations suggest the following boundary conditions for W_1 at $x=L$

$$W_1=W_{1\infty} \quad \text{for } u<0 \tag{13a}$$

$$\partial W_1/\partial x=0 \quad \text{for } u>0. \tag{13b}$$

The second condition allows the solution the freedom to determine the W_1 distribution in the outflow stream. For concreteness, equations (13a) and (13b) will be termed the inflow/outflow boundary condition.

The tube wall ($r=R$) is impermeable to both the gas and the vapor. From this, it readily follows that [2]

$$v=0, \quad \partial W_1/\partial r=0. \tag{14}$$

However, no totally definitive statements can be made about the no-slip boundary condition. The uncertainty arises because $\partial W_1/\partial x\neq 0$ at the tube wall, so that there is a diffusive flux directed axially along the wall. Therefore, the no-slip condition at the wall

$$u=0 \tag{15}$$

will be invoked as an assumption. If there were to be slip, the convective motions would be more vigorous than those corresponding to the no-slip assumption. In this sense, the latter assumption is conservative.

Along the centerline of the tube ($r=0$), the symmetry conditions are represented by

$$v=\partial u/\partial r=\partial W_1/\partial r=0. \tag{16}$$

This completes the formulation of the simplest model for the isothermal case.

The non-isothermal case

The governing differential equations for the non-isothermal case include equations (1)–(4) plus energy conservation

$$\rho^* c_p^* [u(\partial T/\partial x) + v(\partial T/\partial r)] = k^* \nabla^2 T + \rho^* D^* (c_{p1} - c_{p2})(\nabla W_1 \cdot \nabla T). \quad (17)$$

In this equation, ρ^* is as defined by equation (5), while other reference quantities are introduced as

$$W_1^* = (W_{1\infty} + W_{1s})/2, \quad T^* = (T_\infty + T_s)/2 \quad (18)$$

and

$$c_p^* = W_1^* c_{p1} + (1 - W_1^*) c_{p2}. \quad (19)$$

The viscosity μ^* and thermal conductivity k^* were taken as those of the gas corresponding to T^*, and D^* is from equation (6). Note that account has been taken of the energy transported by diffusion of mass (last term of equation (17)). It should also be noted that the variation of the mixture density, which drives the natural convection, now responds to temperature variations in addition to mass fraction variations (see equation (7)).

As noted in the Introduction, the non-isothermal model to be dealt with in the simplest model category is highly oversimplified. In particular, the temperature at the liquid surface will be prescribed parametrically, without consideration of the processes which contribute to establishing its value. Those processes will be dealt with later. The present model is defined at $x = 0$ by

$$T = T_s \quad (20)$$

with an adiabatic tube wall ($r = R$)

$$\partial T/\partial r = 0 \quad (21)$$

the inflow/outflow closure condition at the top of the tube ($x = L$)

$$T = T_\infty \quad \text{for } u < 0 \quad (22a)$$

$$\partial T/\partial x = 0 \quad \text{for } u > 0 \quad (22b)$$

and symmetry at the centerline ($r = 0$)

$$\partial T/\partial r = 0. \quad (23)$$

This completes the description of the simplest non-isothermal model.

Numerical aspects

The discretization of the governing differential equations follows the practice described in ref. [10]. The solution domain was subdivided into a number of non-overlapping control volumes, and the differential equations were integrated over each control volume. This procedure is conventional and need not be elaborated. The discretized equations were solved as an adaptation of the SIMPLER numerical scheme, with the block correction of ref. [11] incorporated to speed convergence of the iterative procedure.

The computations were performed on a 30×21 non-uniform grid, respectively in the x- and r-directions. The number of grid points was determined by trial runs aimed at finding grid-independent solutions. For the layout of the grid, a two-step process was employed. First, solutions were obtained for a uniform grid. Then, based on the velocity distributions from these solutions, the grid was redeployed on a point-by-point basis in order to accommodate locally rapid variations.

As is standard for elliptic-type natural convection problems, substantial underrelaxation was required to achieve convergence. Convergence was also aided by first running solutions for a sparse grid and then using these solutions as input to a refined grid, the solutions of which were, in turn, used as input to a still finer grid.

Parameters

The numerical solutions to be reported here were performed using input conditions representative of those encountered during the experiments—but not the specific conditions of any given data run. Since the experiments were performed for the evaporation of water into air which contains water vapor, the numerical work also dealt with this situation. For the isothermal case, the input parameters were

$$T = T_\infty = 22°\text{C}, \quad p_\infty = 740 \text{ mm Hg}, \quad \phi_\infty = 0.3, \quad 0.35 \leqslant L/d \leqslant 3. \quad (24)$$

Note that the relative humidity ϕ was specified instead of the mass fraction W_1. This is because the magnitudes of the former are more familiar than those of the latter. For the non-isothermal case, T_∞, p_∞, and ϕ_∞ were as in equation (24), with the added conditions

$$19.5°\text{C} \leqslant T_s \leqslant 22°\text{C}, \quad L/d = 1. \quad (25)$$

It is relevant to compute the Rayleigh numbers which correspond to these conditions. Since the natural convection motions considered here are both mass fraction and temperature driven, it is proper to use a Rayleigh number based on a density difference rather than on a temperature difference

$$Ra = [g\rho^*(\rho_\infty - \rho_s)d^3/\mu^{*2}]Sc \quad (26)$$

where the starred quantities have already been defined. Note that the Rayleigh number is positive when $\rho_s < \rho_\infty$. The Schmidt number Sc is 0.60 for the water vapor/air system.

For the isothermal case, $Ra = 9.2 \times 10^3$, while for the non-isothermal case, Ra ranges from 9.2×10^3 to -3.9×10^3, the negative value indicating that ρ_s exceeds ρ_∞.

The results for the evaporation rate $\dot{M}$ will be reported in terms of the mass transfer coefficient K and the Sherwood number Sh. The evaporation rate $\dot{m}$ per unit area at any location on the liquid surface is given by the sum of the convective and diffusive components

$$\dot{m} = \rho_{1s} u - \rho_s D^* (\partial W_1/\partial x)_{x=0} = \rho_s u \quad (27)$$

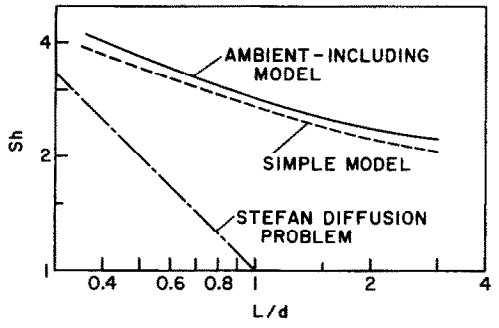

FIG. 1. Sherwood number results for isothermal evaporation.

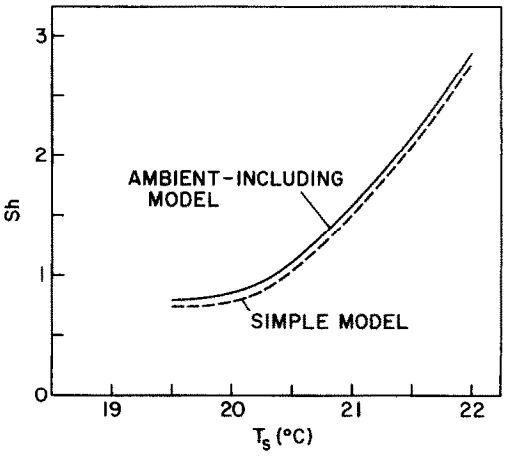

FIG. 2. Response of the Sherwood number to parametric variations of the temperature of the liquid surface.

where the rightmost member follows by employing equation (11). Then

$$\dot{M} = \int_0^R 2\pi r \dot{m}\, dr. \tag{28}$$

The mass transfer coefficient and Sherwood number are defined as

$$K = (\dot{M}/A)/(\rho_{1s} - \rho_{1\infty}), \quad Sh = Kd/D. \tag{29}$$

Here, A denotes the tube cross-sectional area πR^2, while ρ_{1s} and $\rho_{1\infty}$ are the vapor densities at the liquid surface and in the ambient. For the simple models now being considered, ρ_{1s} is constant along the liquid surface. However, for certain models to be employed later, ρ_{1s} varied slightly with the radial coordinate r. For those cases, the surface-average value was used, i.e.

$$\int_0^R \rho_{1s} 2\pi r\, dr/\pi R^2. \tag{30}$$

Numerical results

The evaporation rate results for the simplest models, as conveyed by the Sherwood number, are presented in Figs. 1 and 2. The first of these figures is for the isothermal case, while the second figure is for the non-isothermal case. Both figures are for the evaporation of water into air which contains water vapor. The parameter values for the isothermal case are set forth in equation (24), while the additional specifications for the non-isothermal case are conveyed by equation (25).

In Fig. 1, the Sherwood number is plotted as a function of the length–diameter ratio L/d of the space between the liquid surface and the top of the tube. In addition to the Sh vs L/d results for the simple isothermal model (dashed line), the figure also includes a dashed-dot line representing the solution for the Stefan diffusion problem

$$Sh = 1/(L/d). \tag{31}$$

The solid line represents a more complex isothermal model to be discussed later.

Both the Stefan model and the present simple model are in trendwise agreement that the Sherwood number decreases as the distance between the liquid surface and the top of the tube increases. However, the decrease in Sh is much more rapid for the Stefan case. For the range of L/d covered in the figure, the Sherwood numbers are substantially higher for the present model, which includes natural convection, than for the Stefan model, in which only diffusion is taken into account. For example, for $L/d = 1$, the respective Sherwood numbers are 2.7 and 1. It is seen, therefore, that natural convection plays a decisive role for the range of L/d depicted in the figure. This finding has already been set forth in ref. [2] for other operating conditions.

Extrapolation of the Sh vs L/d curves to lower L/d values suggests a crossing of the curves so that the Stefan results will exceed those of the present model. Indeed, for the Stefan model, which is one-dimensional, $Sh \to \infty$ as $L/d \to 0$. On the other hand, the small L/d behavior of the present two-dimensional model cannot so easily be assessed. This issue requires further investigation.

Figure 2 shows the response of the Sherwood number to parametric variations of the temperature T_s of the liquid surface for a fixed value of $L/d = 1$. The dashed line represents the simple model, while the solid line is for a more complex model to be considered later. Since $T_\infty = 22°C$, the Sh value corresponding to $T_s = 22°C$ is equal to that of Fig. 1 for the isothermal case.

As expected, the Sherwood number decreases as the water surface temperature is parametrically reduced. This is because the lower temperature opposes the species-related upward increase of the mixture density which furnishes the primary impetus for the natural convection. The sensitivity of Sh to decreasing T_s diminishes as Ra approaches zero. For $T_s \leqslant 20°C$, Ra is negative and Sh is quite insensitive to T_s.

Attention will now be turned to the pattern of fluid flow. Figure 3(a) displays a set of streamlines for the isothermal case with $L/d = 1$. These streamlines show that fluid from the ambient enters the tube in an annular region adjacent to the wall and that fluid

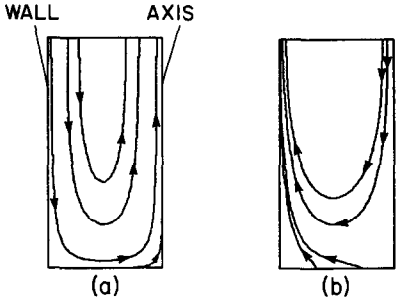

FIG. 3. Patterns of fluid flow in the gas–vapor space computed from the simplest isothermal and non-isothermal models: (a) isothermal case, (b) non-isothermal case with $T_s = 20.5°C$.

leaves the tube in a circular zone which surrounds the axis. The streamline emanating from the liquid surface is indicative of the mass that is being added to the gas–vapor mixture due to evaporation.

Figure 3(b), which corresponds to the non-isothermal case with $T_s = 20.5°C$ and $L/d = 1$, displays a pattern that is markedly different from that of Fig. 3(a). In particular, the inflow from the ambient to the tube occurs adjacent to the axis, while the outflow occurs adjacent to the wall.

These behaviors are reflected in the velocity profiles displayed in Figs. 4 and 5. In these figures, the axial velocity u is embedded in the dimensionless group ud/ν which resembles a local Reynolds number. For selected axial stations defined by x/L, ud/ν is plotted as a function of the dimensionless radial coordinate r/R.

Figure 4 is for the isothermal case for $L/d = 1$. All the profiles are of the two-lobe type. The positive lobe, representing an axial upflow, extends from the tube axis to $r/R \sim 0.52$, and the negative lobe, representing downflow, extends from $r/R \sim 0.52$ to the tube wall. Although the magnitudes of the velocities in both lobes increase with increasing x/L, the integral

$$\int ru\,dr$$

across the section is the same for all profiles in the set.

The velocity profiles displayed in Fig. 5(a) are for the non-isothermal case with $T_s = 21°C$ and $L/d = 1$. These profiles are similar in form to those of Fig. 4 for the isothermal case, but the magnitudes of the velocities are significantly diminished, reflecting the weakened buoyancy which results from the opposing effects of mass fraction and temperature on the density variation.

In Fig. 5(b), the non-isothermal case with $T_s = 20.5°C$ and $L/d = 1$ is displayed. Here, the velocity magnitudes have diminished so much that only the profile with the largest velocities, that at $x/L = 1$, need be plotted to convey the relevant information. In addition to the decreased magnitude, the two lobes are reversed. The inner lobe is now a region of negative velocity, while the outer lobe is a region of positive velocity.

ASSESSMENT OF THE ROLE OF THE AMBIENT

In the foregoing simple models, the interactions between the tube and the ambient were avoided by judicious selection of the boundary conditions at the open top of the tube. Consideration will now be given to an assessment of the effect of those interactions.

The ambient-including model

The description of the model used in the assessment is facilitated by reference to Fig. 6. As seen there, the ambient is modeled as a large cylindrical region the height L' and radius R' of which will be varied parametrically. Also shown in the diagram is the portion of the tube between the liquid surface and the open top, the height and radius of which are L and R as before. In the model now under consideration, the liquid continues to play a passive role and is, therefore, not shown in the diagram. Owing to the assumed axisymmetry, only half of the solution domain is depicted in Fig. 6 (note that the left-hand boundary is the axis of symmetry).

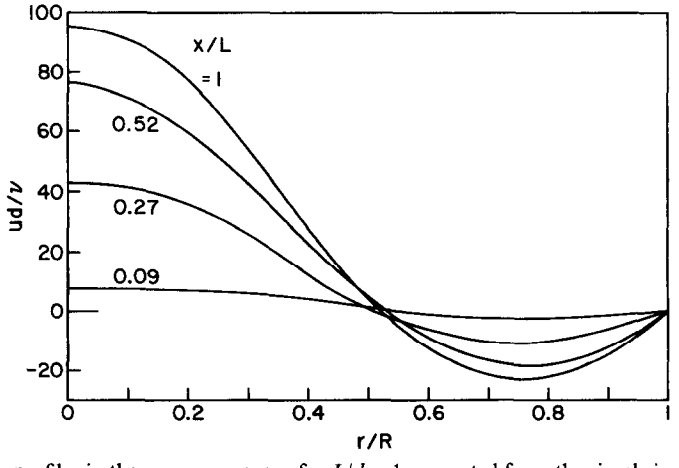

FIG. 4. Velocity profiles in the gas–vapor space for $L/d = 1$ computed from the simple isothermal model.

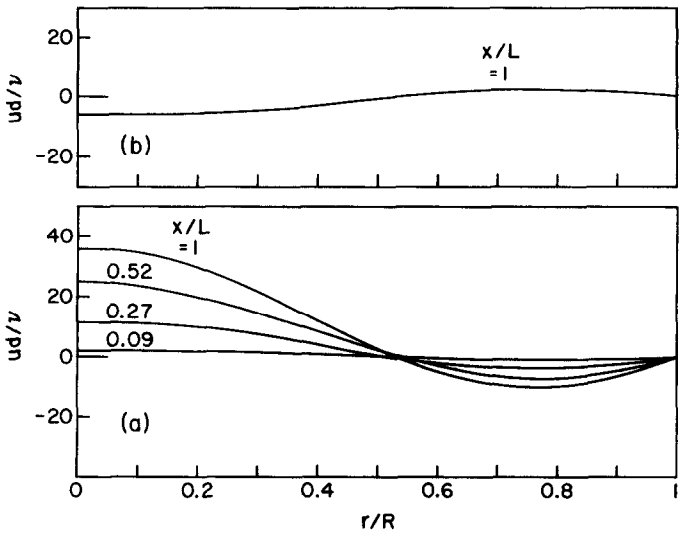

FIG. 5. Velocity profiles in the gas–vapor space for $L/d = 1$ computed from the simple non-isothermal model: (a) $T_s = 21°C$, (b) $T_s = 20.5°C$.

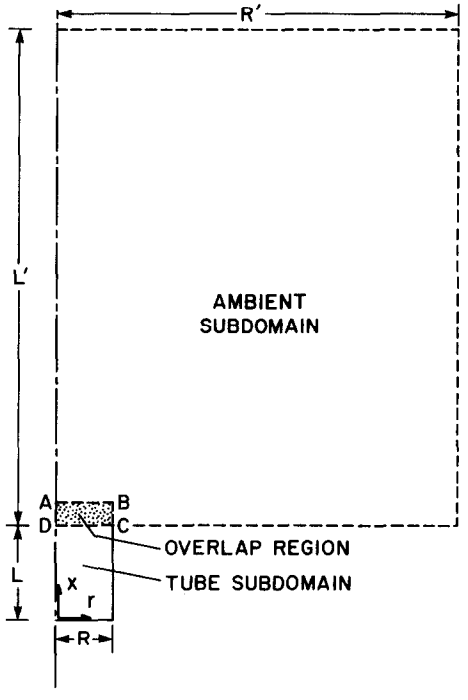

FIG. 6. Solution domain used for modeling the role of the ambient.

The solution domain is subdivided into two parts. This two-subdomain treatment enabled a much larger number of grid points to be used than would have been possible had the entire solution domain been treated as a single unit. The ambient subdomain is a cylinder of height L' and radius R'. However, the tube subdomain includes not only the tube itself but also a disk-like region, shown speckled in Fig. 6, situated atop the tube. Indeed, the speckled region, labeled ABCD, belongs to both the tube subdomain and the ambient subdomain. It is, therefore, a region of overlap.

The reason for the overlap is to facilitate a solution pattern consisting of successive visitations to each subdomain. At the conclusion of each such visit, the boundary conditions for the upcoming visit to the other subdomain are identified. The overlap region facilitates the identification, as will be detailed shortly.

The governing differential equations are common to the two subdomains and are identical to those already stated for the simple models. For the isothermal case, the relevant equations are equations (1)–(4), while for the non-isothermal case, equation (17) is added.

The tube-subdomain boundary conditions at the liquid surface, at the tube wall, and at the axis are the same as those for the simple models. These are described by equations (9), (11), and (14)–(16) for the isothermal case, with equations (20), (21), and (23) added for the non-isothermal case. Note that the non-isothermal treatment continues to incorporate the many oversimplifications that were employed earlier but which will be lifted in the next section.

The foregoing specification does not include boundaries AB and BC which form the top of the tube subdomain. For now, it may be stated that the velocities u and v, the mass fraction W_1 and, if appropriate, the temperature T are specified on these boundaries. The manner in which the specification is accomplished will be evident when the solution pattern is described.

The boundary conditions for the ambient subdomain will now be considered. Excluding the axis and the tube opening CD, on the remaining boundaries the velocity field is required to obey

$$\partial u/\partial n = \partial v/\partial n = 0 \qquad (32)$$

where n is the normal to the boundary. These conditions were selected so as not to impose significant constraints on the boundaries of the velocity field.

On the same boundaries, under the assumption that interactions with the tube have died away there, it was assumed that

$$W_1 = W_{1\infty}, \quad T = T_\infty. \tag{33}$$

Along the axis

$$v = \partial u/\partial r = \partial W_1/\partial r = \partial T/\partial r = 0. \tag{34}$$

At the boundary CD of the domain, it suffices for now to state that u, v, W_1, and, if appropriate, T are specified.

Numerical aspects

For the numerical work, values of T_∞, p_∞, ϕ_∞, L/d, and T_s (for the non-isothermal case) are specified. The governing differential equations are discretized as before (following the practice of ref. [10]) and are solved using the SIMPLER scheme supplemented by the block correction. The computations are begun in the tube subdomain. For this first round of computations, u, v, W_1, and T (for the non-isothermal case) are assigned on AB and BC. Then, 15 iterations are performed in the tube subdomain. The values of u, v, W_1, and T on CD from the fifteenth iteration are then stored and used as the boundary conditions for the upcoming visit to the ambient subdomain. Fifteen iterations are then carried out in the ambient subdomain, and, from the last of these, u, v, W_1, and T on AB and BC are identified and stored for use as boundary conditions for the upcoming set of 15 iterations in the tube subdomain. The process is continued until convergence. Note how the overlap of the two subdomains simplifies the updating of the boundary conditions.

The foregoing description of the pattern of the computations will be completed by taking note of certain relevant details. The first has to do with global mass conservation for the tube subdomain, which requires that the rate of mass outflow be equal to the sum of the rate of mass inflow plus the rate of evaporation at the liquid surface. If the velocities on AB and BC were held fixed throughout all 15 iterations of a given set, global conservation would not be fulfilled because the rate of evaporation varies from iteration to iteration. To deal with this issue, at the end of each iteration in the tube subdomain, note is taken of the rates of inflow, outflow, and evaporation, and the following ratio is formed:

$$(\text{inflow} + \text{evaporation})/\text{outflow}. \tag{35}$$

Then, all the velocities on the outflow portion of the boundary are multiplied by this ratio, thereby satisfying global conservation.

The other issue to be noted is that in the SIMPLER scheme, the grid for the velocity is staggered relative to the so-called main grid which is used for the pressure, the mass fraction, and the temperature. As a result of this staggering, u velocities are not directly available along BC, and v velocities are not directly available along AB and CD. The needed velocities were obtained via linear interpolation [1], with proper account being taken of the staggering.

A systematic numerical examination was made of the effect of the size of the ambient subdomain. This examination was performed for the isothermal case with T_∞, p_∞, and ϕ_∞ specified by equation (24) and with $L/d = 1$. Initial computational experiments established that the Sherwood number which characterizes the evaporation rate was insensitive to the height L' of the ambient subdomain when $L' > 6R$ (R = tube radius). Then, with L' fixed at $6R$, the radial dimensions of the subdomain were assigned values $R' = 3R$, $6R$, $8R$, and $10R$. The corresponding grid point populations were (axial × radial) 20×30, 20×34, 20×36, and 20×38. In the tube subdomain, a 34×21 grid was used. The grid points were deployed nonuniformly to accommodate regions of relatively high gradients.

The computed Sherwood numbers corresponding to $R'/R = 3$, 6, 8, and 10 (for $L' = 6R$) are 2.837, 2.836, 2.835, and 2.835. These numbers are identical by any practical measure, so that all of the examined ambient domain sizes appear to be equally satisfactory. However, the $6R \times 6R$ ambient domain corresponded to the minimum computational time for convergence, so that it was adopted for all of the final runs.

The foregoing assessment of the size of the ambient subdomain was performed for $L/d = 1$. The final computer runs included a range of L/d values. For all $L/d \neq 1$, the grid point population and deployment in the overlap region was maintained identical to that for $L/d = 1$.

Numerical results

For the isothermal case, the ambient-including model was numerically implemented for the same conditions, expressed by equation (24), as were used for the simple model. The Sherwood number result for $L/d = 1$ has already been mentioned, namely, 2.836. This may be compared with the value of 2.727 from the simple model. The difference between the two results is about 4%.

A comparison between the Sherwood numbers for the ambient-including and simple models is presented in Fig. 1 (solid and dashed lines, respectively) over the investigated range of L/d between 0.35 and 3. As seen in the figure, the two models yield a virtually identical variation of Sh with L/d. Typically, the Sh values for the ambient-including model are about 5% higher than those for the simple model. This is a modest and acceptable deviation, especially when note is taken of the significant reduction in computational complexity and effort that are dividends of the simple model.

For the non-isothermal case, the Sherwood numbers from the ambient-including and simple models are compared in Fig. 2. These results are for the T_∞, p_∞, and ϕ_∞ of equation (24), with $L/d = 1$ and T_s ranging between 19.5 and 22°C. Once again, the two models yield distributions that track each other with

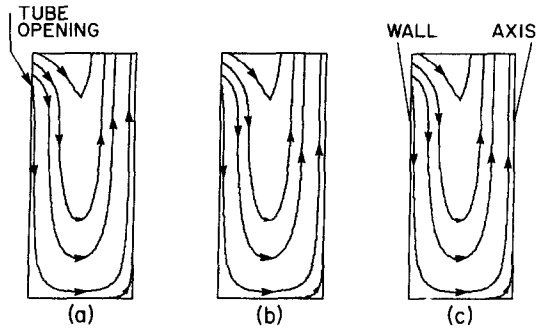

FIG. 7. Patterns of fluid flow in the gas–vapor space computed from the ambient-including isothermal model for various ambient subdomain sizes (axial × radial): (a) $6R \times 3R$, (b) $6R \times 6R$, and (c) $6R \times 8R$.

high fidelity. As was true in the isothermal case, the *Sh* values for the ambient-including model are consistently higher than those for the simple model. The deviations are, again, in the 5% range.

The Sherwood number results for both the isothermal and non-isothermal cases provide strong evidence that the suppression of tube–ambient interactions as accomplished in the simple models is an acceptable practice. This suggests that the closure conditions that were used at the tube opening for the simple models might profitably be used when the many complexities of non-isothermal evaporation are dealt with, as in the forthcoming section of the paper.

Fluid flow patterns in the form of streamline maps will now be exhibited for the isothermal case. Figures 7(a)–(c) show the tube subdomain for $L/d = 1$ for ambient subdomains of dimensions $6R \times 3R$, $6R \times 6R$, and $6R \times 8R$, respectively. Note that the tube subdomain includes not only the portion of the tube between the liquid surface and the open top but also a disk-like part of the ambient situated just above the tube. The location of the tube opening is identified in Fig. 7, and the streamline segments which lie above the opening belong to the ambient.

An overview of Fig. 7 indicates that the streamline pattern is virtually independent of the investigated variations of the size of the ambient subdomain. This finding reinforces a similar finding that resulted from a comparison of Sherwood numbers. It is also relevant to compare Fig. 7 with Fig. 3(a), the latter corresponding to the simple model. If consideration is restricted to the in-tube portion of the streamlines of Fig. 7, a marked similarity is seen to exist with the streamlines of Fig. 3(a). The only noteworthy difference is the slight transverse velocity component in the flow entering the opening of the tube—present in the ambient-including model and absent in the simple model.

The flow pattern in the ambient is exhibited in Fig. 8. As seen there, the fluid entering the tube from the ambient is drawn from the side along nearly horizontal streamlines which subsequently turn downward into the tube opening. The fluid which exits the tube forms a vertical jet which maintains its identity

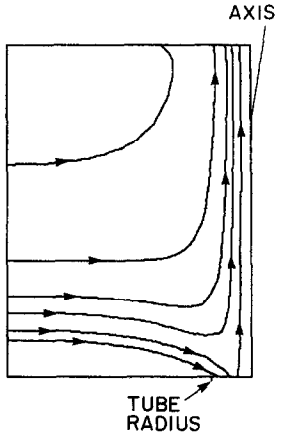

FIG. 8. Pattern of fluid flow in the ambient computed from the ambient-including isothermal model.

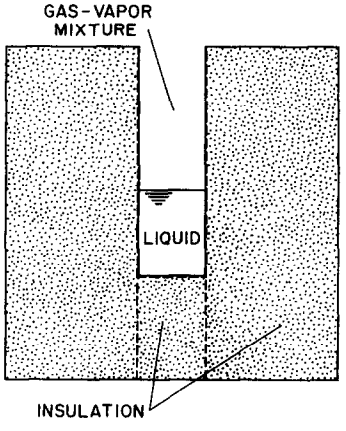

FIG. 9. Schematic diagram of a representative experimental setup for studying non-isothermal evaporation.

throughout the height of the ambient subdomain. The jet entrains fluid from the side, fluid which is drawn from the far field along horizontal streamlines which later turn to conform to the vertical orientation of the jet.

IN-DEPTH MODELING OF THE NON-ISOTHERMAL CASE

To introduce the upcoming non-isothermal modeling effort, it is useful to briefly consider a typical experimental setup for non-isothermal evaporation studies such as those of ref. [1]. Such a setup is illustrated in Fig. 9. As seen there, a pool of liquid (water) partially fills an open-topped, non-metallic tube. The tube is situated in a large, closed cardboard container filled with a very low conductivity insulating material (a powder). To facilitate the containment of the insulation and the positioning of the tube, a thin-walled cardboard liner (depicted by the dashed lines in the figure) is used to create a cavity which houses the tube.

As discussed in the Introduction, four models, successively with ascending complexity and fidelity to reality, will be employed to deal with the non-isothermal evaporation problem. To enable these new

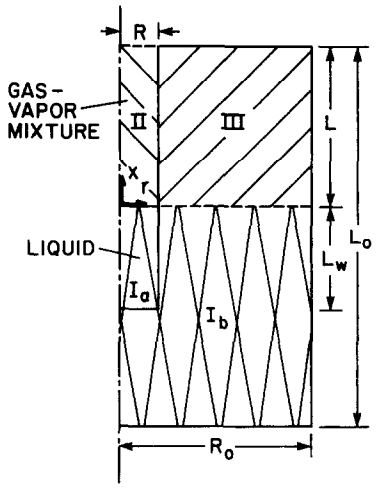

FIG. 10. Computational domains used in the modeling of non-isothermal evaporation.

features to be taken into account within the capabilities of the available computational resources, direct interactions between the tube and the ambient will be suppressed by the use of the closure conditions used for the simple models. This practice was explored in the preceding section of the paper and found to be acceptable. There, a correction factor of 5% was found applicable for converting *Sh* values for non-ambient-including models to *Sh* values for ambient-including models. Such a correction factor will be used for the Sherwood number results to be obtained in this section of the paper.

In the first three of the four models to be examined, neither the thickness of the tube wall nor of the liner will be taken into account. Rather, the inner boundaries of the insulation will be assumed to coincide with the inner walls of the tube. In the fourth model, both the tube wall and the liner will be included.

The computational domains used in the modeling are depicted in Fig. 10 along with the coordinates and dimensional nomenclature. The diagram shows the gas–vapor, liquid, and insulation regions which were pictured in Fig. 9. Because of axisymmetry, only the right half of what appeared in Fig. 9 is included in Fig. 10 (the left-hand boundary of Fig. 10 is the symmetry axis).

To facilitate the numerical work, the solution domain was divided into three subdomains, respectively designated as I, II, and III. Subdomain I includes both the liquid pool and the lower part of the insulation (i.e. below the level of the liquid surface), and the designations I_a and I_b have been employed to identify these two regions of I. Subdomain II corresponds to the gas–vapor mixture which fills the space between the liquid surface and the tube opening, while subdomain III is the upper part of the insulation.

Other subdivisions are, of course, possible. Indeed, a seemingly more natural subdivision would assign a separate subdomain to the gas–vapor, the liquid, and the insulation regions. The general purpose computer codes used here readily accommodate cylindrical regions such as those occupied by the gas–vapor mixture and the liquid, and annular regions are also well accommodated. However, the odd-shaped insulation region (a cylinder with a partially penetrating hole) is not handled efficiently. Because of this, only cylindrical or annular subdomains were considered.

The fact that one of the selected subdomains—subdomain I—includes regions containing different materials (i.e. liquid and insulation) poses no difficulties for the present computer codes. Both continuous and abrupt variations of the thermophysical properties can be handled. At a control volume face where a property discontinuity occurs, the harmonic mean value of the property is used [12]. Furthermore, a solid can be treated as a fluid of infinite viscosity.

The successive non-isothermal models will now be formulated.

Model NI 1

This model includes mass, heat, and momentum transfer in the gas–vapor mixture, heat conduction in the insulation, and heat conduction in the liquid pool.

The governing differential equations for the gas–vapor region, subdomain II, are expressed by equations (1)–(4) and (17). In subdomain III (insulation), the heat conduction is governed by

$$k_{ins}\nabla^2 T = 0. \tag{36}$$

For subdomain I (liquid and insulation), the heat conduction is described by

$$k^{**}\nabla^2 T = 0 \tag{37a}$$

where

$$k^{**} = k_{wtr} \text{ in } I_a, \quad k^{**} = k_{ins} \text{ in } I_b. \tag{37b}$$

The numerical value of k_{wtr} was the mean of the thermal conductivities of water at $r = R/2$ on the upper and lower bounding surfaces of the water. Owing to the inherent uncertainty of k_{ins}, a representative value was used.

Attention will now be turned to the boundary conditions and to the conditions of continuity at the interfaces of the solution domains. At the external boundaries of the insulation

$$T = T_\infty. \tag{38}$$

The rationale for this specification is that the thermal resistance of the insulation is much greater than that of the convection external to the insulation (Biot number much greater than one). If the insulation container rests on a solid surface, the surface is also assumed to be at T_∞.

At the tube opening, the boundary conditions from the simple models will be adopted, namely, equations (12) for the velocities, (13) for W_1, and (22) for the temperature. This practice has been amply justified. Along the symmetry axis, the boundary conditions for subdomain II are conveyed by equations (16) and

(23), while for subdomains I_a and I_b, equation (23) is applicable.

The two preceding paragraphs have dealt with the external boundaries of the solution domain as a whole. Consider now the interface between subdomains I_b and III, where temperature and heat flux continuity must both be satisfied locally. Both these conditions can be incorporated into a single difference equation. To this end, at any r at which there is a vertical array of grid points, let $T_{int}(I_b/III)$, T_{III}, and T_{I_b} respectively denote the temperatures at a point on the interface between I_b and III, at a point in subdomain III at a distance δ_{III} above the interface, and at a point in subdomain I_b at a distance δ_{I_b} below the interface. Then

$$k_{ins}[T_{III} - T_{int}(I_b/III)]/\delta_{III} = k_{ins}[T_{int}(I_b/III) - T_{I_b}]/\delta_{I_b} \quad (39)$$

or

$$T_{int}(I_b/III) = (\delta_{I_b} T_{III} + \delta_{III} T_{I_b})/(\delta_{I_b} + \delta_{III}). \quad (40)$$

With regard to the interface between subdomains II and III, the local implementation of temperature and heat flux continuity leads to an equation for T_{int} (II/III) similar to equation (40), with the main difference being that the thermal conductivities k^* and k_{ins}, respectively for the gas–vapor mixture and the insulation, appear. On the II side of the II/III interface, the boundary conditions for the velocity and the mass fraction are as conveyed by equations (14) and (15).

The other interface to be considered is that between subdomains I_a and II. If account is taken of the evaporation on the II side of the interface, continuity of energy at any location on the interface takes the form

$$-k^{**}(\partial T/\partial x)_{I_a} = -k^*(\partial T/\partial x)_{II} + (\rho u h_{fg})_{II} \quad (41)$$

where $k^{**} = k_{wtr}$ and k^* is the conductivity of the gas, both at already discussed reference states. The velocity u appearing in equation (41) is given by equation (11), applied locally. The finite difference form of equation (41) yields an equation for $T_{int}(I_a/II)$.

On the II side of the I_a/II interface, the velocity conditions are stated by equations (9) and (11), now applied locally, and the mass fraction condition of equation (9) is also applied locally. Since the solution in subdomain II is to be obtained iteratively, it was found convenient to take the interface values of W_1 and u from the preceding iteration. Note that W_1 is determined assuming that each location on the interface is a saturation state at temperature $T_{int}(I_a/II)$. The actual determination parallels that discussed following equation (9), with suitable modifications to take account of the fact that the local surface temperature is $T_{int}(I_a/II)$ and not T_∞.

The pattern of solution is based on successive visits to subdomains III, I, and II, in that order. Suppose that this process is in progress and that a new cycle is about to begin. When working in subdomain III, use is made of the previously discussed equations for $T_{int}(I_b/III)$ and $T_{int}(II/III)$ as boundary conditions at the I_b/III and II/III interfaces. Any quantities in these equations which belong to subdomains I_b and II are held fixed at the most recently available values. The temperature field in III, which is a conduction subdomain, is solved to near convergence by line-by-line application of the tridiagonal matrix algorithm in alternate directions.

The action is then transferred to subdomain I which, in this model, is a conduction region and which was solved by the same procedure used for region III. The equations for $T_{int}(I_a/II)$ and $T_{int}(I_b/III)$ served as boundary conditions, with any quantities pertaining to II and III held fixed.

After I is solved, the action goes to II, which is a subdomain where convection occurs. At each visit to II, the SIMPLER algorithm was used to perform 15 iterations. Once again, quantities appearing in the boundary condition equations which belong to other subdomains are held fixed when working in II. Furthermore, as already noted, W_1 and u at the I_a/II interface lagged by one iteration.

After the 15 SIMPLER iterations were completed in II, the action is returned to III, and another cycle is begun.

Solutions were obtained employing uniform grid distributions, except for the radial distribution of points in subdomain I, for which Δr changed at $r = R$. The computations in III were performed with a 25×15 uniform grid (axial $\times$ radial). The grid for I was a 26×36 non-uniform distribution (axial $\times$ radial). The first 21 radial points were uniformly deployed to line up with those of II, while the remaining 15 radial points lined up with those of III. Subdomain II had a 25×21 grid, with the 25 axial points placed to line up with III. The computations were confined to $L/d = 1$.

Model NI 2

The difference between models NI 2 and NI 1 is the inclusion in the former of radiation heat transfer among the bounding surfaces of the gas–vapor region (subdomain II). Consideration is given to radiation because of its competitiveness with natural convection. The radiative transfer was activated by the naturally occurring temperature differences among the water surface, the tube wall, and the ambient.

The net effect of accounting for the radiative transfer is to significantly modify the $T_{int}(I_a/II)$ and $T_{int}(II/III)$ equations. Aside from this, all other aspects of model NI 1 are retained, as is the solution methodology. Therefore, attention will be confined here to describing the basis for the modification of the aforementioned equations.

To facilitate the discussion, reference may be made to Fig. 11, which shows the bounding surfaces of the gas–vapor space (subdomain II). The cylindrical wall of the tube may be regarded as being subdivided into an array of ring-like elements. Each such ring is, in

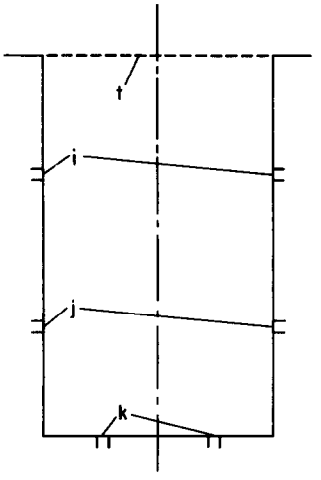

FIG. 11. Diagram relevant to the analysis of radiant interchange in the gas–vapor space.

fact, the exposed face of a surface-adjacent control volume. Two representative ring elements, i and j, are shown in the figure. The water surface is subdivided into an array of annular elements, which are also the exposed faces of control volumes, as illustrated by element k.

To create an enclosure, as is needed for the analysis of radiative interchange, the top of the tube is regarded as being closed by a fictive surface t. This surface behaves like a blackbody absorber and emitter in order to correctly represent the radiative role of the ambient. The ambient is postulated as being a region filled with blackbody radiation corresponding to temperature T_∞, so that the fictive black surface is also assigned the temperature T_∞.

In the experimental setup which motivated the modeling, the tube which contained the evaporating water was made of opaque polyethylene, the emissivity of which is only slightly less than one. Similarly, the emissivity of the water surface is near one. With this, and taking account of the fact that the apparent emissivity of a cavity exceeds the actual emissivity of the surfaces (Chap. 6 in ref. [13]), there is little loss of accuracy in assuming that the side and bottom bounding surfaces of the gas–vapor space are black.

Attention may now be turned to the modification of the equation for $T_{int}(I_a/II)$ which applies locally at the I_a/II interface. The net rate of outflow of energy by radiation per unit area at an annular element such as k (Fig. 11) is

$$q_{rad,k} = \sigma T_k^4 - \sigma T_\infty^4 F_{k-t} - \sum_{side} \sigma T_j^4 F_{k-j}. \quad (42)$$

In this equation, the first term on the right is the radiant energy emitted at k, while the second and third terms represent absorption at k, respectively due to emission at the fictive surface t and at the side wall.

The quantities F_{k-t} and F_{k-j} are angle factors. These are dimensionless numbers between 0 and 1 the value of which represents the fraction of the radiation leaving one surface which arrives at another surface. For example, F_{k-t} is the fraction of the radiation which leaves the annular surface k that arrives at disk t. The numerical values of the needed angle factors are readily obtained from information given in ref. [13].

The inclusion of $q_{rad,k}$ from equation (42) on the right-hand side of equation (41) completes the energy balance at the I_a/II interface. Subsequent discretization yields the equation for $T_{int}(I_a/II)$ (note that T_k and that $T_{int}(I_a/II)$ are one and the same).

To avoid the T^4 nonlinearities inherent in the radiation representation, the following linearization is employed:

$$T^4 = 4(T^-)^3 T - 3(T^-)^4. \quad (43)$$

Here, T^- denotes the temperature at the preceding iteration, while T represents the temperature at the present iteration. When $T = T^-$, as occurs at convergence, then equation (43) is a true identity.

Linearization (43) was applied to T_k^4 and T_j^4 in equation (42) but not to T_∞^4, since T_∞ is a known constant. The linearized form of equation (42) was used in energy balance (41).

The accounting of radiative interchange in the T_{int} (II/III) equation follows the same pattern as was just discussed for $T_{int}(I_a/II)$. The basic step is to introduce a radiation term into the energy balance at the II/III interface. Such a term, appropriate to any surface element i on the interface (Fig. 11), is

$$q_{rad,i} = \sigma T_i^4 - \sigma T_\infty^4 F_{i-t} - \sum_{side} \sigma T_j^4 F_{i-j} - \sum_{bot} \sigma T_k^4 F_{i-k}. \quad (44)$$

Note that the right-hand side includes absorption at i due to emission at the top, side, and bottom bounding surfaces of the space. In the summation over the side surface, there is a term $\sigma T_i^4 F_{i-i}$, which represents emission from element i that is incident on itself.

Equation (44) is linearized in accordance with equation (43) and then introduced into the local energy balance at the II/III interface. After discretization and noting that T_i is synonymous with $T_{int}(II/III)$, the sought-for equation for $T_{int}(II/III)$ is obtained.

This completes the NI 2 model. The computational aspects are the same as those for the NI 1 model. Computations were performed for $L/d = 1$.

Model NI 3

The numerical solutions for models NI 1 and NI 2 revealed that in the liquid pool, the temperature decreased in the vertically upward direction. In those models, the liquid was postulated to be stationary and heat conduction was the only mode of energy transport. In the presence of an upward decreasing temperature, natural convection occurs when the liquid-pool Rayleigh number exceeds a threshold value.

The special feature of model NI 3 is to take account of natural convection in the liquid pool while main-

taining all the other attributes of model NI 2. Attention will now be focused on this new feature.

Before presenting the governing equations for natural convection in the liquid pool, it is relevant to recall from Fig. 10 that the pool occupies only part of subdomain I, namely, region I_a. Since the computer program requires a common set of differential equations for all of subdomain I, it will be expedient to write the equations in generalized form and then to tailor them to regions I_a and I_b by proper selection of the thermophysical properties.

Furthermore, to achieve a concise presentation, the statement of the governing equations will be accomplished by referring to earlier equations and indicating appropriate changes. Conservation of x- and r-momentum is given by equations (1) and (2), with ρ^* and μ^* replaced by ρ^{**} and μ^{**}. Mass conservation is expressed without change by equation (3). Energy conservation is given by equation (17), with ρ^*, c_p^*, and k^* replaced by ρ^{**}, c_p^{**}, and k^{**}, and with the last term on the right deleted.

These equations will now be tailored to subdomains I_a (liquid pool) and I_b (insulation). For the insulation region, set $\mu^{**} \simeq \infty$. This leads to $u = v = 0$, so that heat conduction is the only mode of energy transport, as it should be. Furthermore, in the insulation region, $k^{**} = k_{ins}$.

For the liquid region, ρ^{**}, μ^{**}, c_p^{**}, and k^{**} are water properties obtained by averaging the property values at $r = R/2$ on the upper and lower bounding surfaces of the pool. The density ρ which appears in the body force term of the x-momentum equation was evaluated directly from the density–temperature relation for liquid water, without employing the Boussinesq linearization.

With the specification of the governing equations now complete, the boundary conditions relevant to region I_a may be considered. Nothing special need be done at the interface between regions I_a and I_b because everything is taken care of by the specified thermophysical properties (e.g. the zero velocity values in I_b are imposed at the I_a/I_b interface). At the tube axis, $v = \partial u/\partial r = 0$ is imposed, along with $\partial T/\partial r = 0$ from before.

The boundary conditions at the I_a/II interface (i.e. the liquid surface) require greater attention. The u velocity of equation (11) for the II side of the interface continues to apply and, strictly speaking, the u velocity on the I_a side should be given by $u_{I_a} = u_{II}(\rho_{II}/\rho_{I_a})$. However, $\rho_{II}/\rho_{I_a} \sim 0.001$ for water evaporating into air. Therefore, it appears reasonable to take $u_{I_a} \simeq 0$, which immobilizes the interface and makes the problem quasi-steady.

The value of the v velocity at the interface, which is common to both the I_a and II sides, is obtained from the continuity of shear stress

$$\mu^{**}[(\partial v/\partial x)+(\partial u/\partial r)]_{I_a} = \mu^{*}[(\partial v/\partial x)+(\partial u/\partial r)]_{II}. \quad (45)$$

In accordance with the foregoing, $(\partial u/\partial r)_{I_a} \simeq 0$. With this and with the discretization of equation (45), an equation for $v(I_a/II)$ emerges. This completes the discussion of the boundary conditions.

The numerical work for this model involves one major change relative to that for models NI 1 and NI 2. The new feature is that convection now occurs in subdomain I. Correspondingly, at each visit to I, the SIMPLER algorithm was used to perform 15 iterations. Aside from this change, the other aspects of the numerical work were the same as for the preceding models.

Model NI 4

The final stage of the modeling is aimed at taking account of the presence of the tube wall and of the liner which served to contain the insulation. This is accomplished in the forthcoming model NI 4, which also continues to include all features of model NI 3.

The liner, depicted by the dotted line in Fig. 9, is external to the tube. Although their thickness and composition were specific to the companion experiments, it was felt worthwhile to assess the effect of these elements because they do represent a link with reality. In principle, since only heat conduction is involved, incorporation of these elements into the finite difference solution method should have presented no difficulty. However, since the combined thickness of the tube wall and the liner (0.2 cm plus 0.1 cm) was slightly smaller than the radial step Δr in the adjacent insulation, some refitting of the grid was necessary.

The details of the refitting are conveyed in ref. [1]. The net result was that for the tube side wall and the liner, the radial grid-point deployment included points at the inner surface of the tube, at the tube–liner interface, and at the outer surface of the liner. For the bottom wall of the tube and the disk-like liner beneath it, a similar positioning of points was used. Considerable pains were taken to verify the independence of the evaporation rate from the layout of the grid points. The k value of the tube was 0.4 W m^{-1} K^{-1}, while that for the liner (which was made from a conventional manila folder) was 0.14 W m^{-1} K^{-1}.

Numerical results

The numerical solutions were carried out for the representative operating conditions $T_\infty = 22°C$, $p_\infty = 740$ mm Hg, and $\phi_\infty = 0.3$, which are the same as those of equation (24). The geometry of the system, specified in terms of the nomenclature of Fig. 10, is defined by: $R = 3.05$, $d = 6.1$, $L = 6.1$, $L_w = 14.2$, $L_0 = 30$, $R_0 = 15$, tube wall thickness = 0.2, and liner thickness = 0.1, where all dimensions are in cm. From the foregoing, it is seen that $L/d = 1$. These dimensions were chosen to model the apparatus used in the complementary experiments.

The numerical solutions yielded the mass transfer coefficient K and the Sherwood number Sh as defined by equation (29), in which $\dot{M}$ is the rate of evaporation

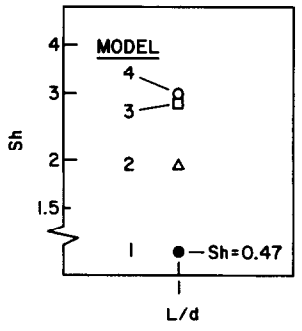

FIG. 12. Sherwood number results for the various non-isothermal models.

and ρ_{1s} is the surface-averaged value obtained from equation (30).

The Sherwood number results are presented in Fig. 12, where they are parameterized by the model number. The plotted points include the 5% correction factor (an increase) that was developed earlier to account for the approximate treatment of the interactions between the tube and the ambient. From the figure, it is seen that model NI 1 yields a very low value of the Sherwood number (i.e. $Sh = 0.47$) and that major increases occur between models NI 1 and NI 2 and between models NI 2 and NI 3. There is only a slight increase between models NI 3 and NI 4.

The aforementioned characteristics of the Sherwood number results are entirely plausible. To establish plausibility, reference may be made to Fig. 2, where it was demonstrated that the Sherwood number decreases as the temperature of the surface of the liquid is depressed relative to the ambient temperature. Among the cases exhibited in Fig. 12, model NI 1 possesses the largest thermal resistance between the ambient and the liquid surface and, correspondingly, the greatest surface temperature depression and the lowest Sherwood number.

The participation of radiative transfer, first incorporated into the model of case NI 2, provides an additional path for heat transfer and significantly decreases the thermal resistance and the temperature depression, with a consequent major increase of the Sherwood number. Natural convection in the liquid pool, activated in model NI 3, further decreases the resistance and the depression, and thereby gives rise to a further significant increase in the Sherwood number. The activation of the tube wall and liner heat conduction tends, primarily by axial conduction, to decrease the resistance, but the change is small and the increase in the Sherwood numbers between models NI 3 and NI 4 is also small.

The presentation of results will conclude with the velocity profiles for the gas–vapor space for model NI 4 (the most complete model). These results are displayed in Fig. 13, where the profiles are parameterized by the axial station x/L ($x/L = 0$ at the liquid surface and $x/L = 1$ at the tube opening). From Fig. 13, it is seen that the direction of fluid flow in the core of the tube is downward, whereas adjacent to the walls the fluid flow is upward. On the basis of information presented in Fig. 3 and in Figs. 4 and 5, the flow pattern of Fig. 13 suggests that thermal effects have overridden the species-related buoyancy which induces an oppositely directed flow pattern.

CONCLUDING REMARKS

The modeling and computational work performed here for the evaporation of a liquid from a partially filled cylindrical tube has provided a set of definitive conclusions. First, Sherwood number results of acceptable accuracy can be obtained without having to extend the numerical solutions into the ambient above the tube. The use of closure conditions at the tube opening expressed by equations (12), (13), and (22) enables the ambient to be excluded from the solution domain. Second, the Sherwood number

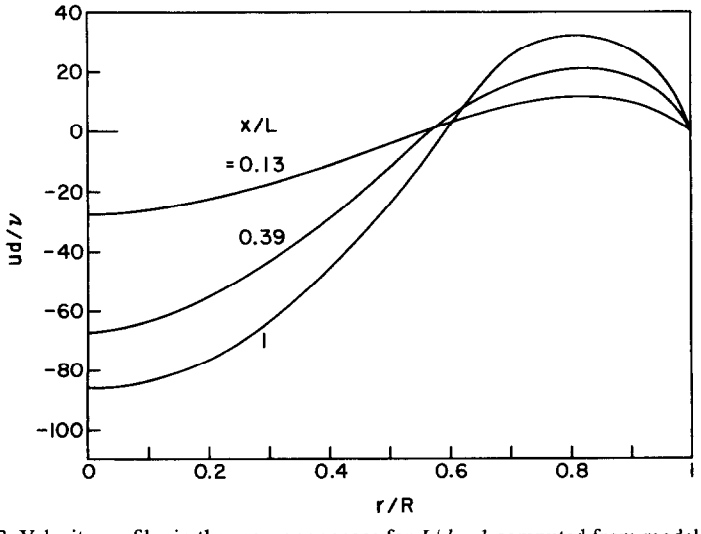

FIG. 13. Velocity profiles in the gas–vapor space for $L/d = 1$ computed from model NI 4.

decreases as the temperature at the surface of the liquid pool is depressed relative to the ambient temperature. The extent of the depression is related to the magnitude of the thermal resistance between the ambient and the liquid surface.

Radiative interchange among the bounding surfaces of the gas–vapor space and the ambient significantly decreases the temperature depression at the liquid surface and brings about a major increase in the Sherwood number. Natural convection in the liquid pool also decreases the thermal resistance and causes a further substantial Sherwood number increase.

REFERENCES

1. G. A. Nunez-Testa, Evaporation in the presence of isothermal and non-isothermal natural convection, Ph.D. thesis, Department of Mechanical Engineering, University of Minnesota, Minneapolis, Minnesota (1986).
2. E. M. Sparrow, G. A. Nunez and A. T. Prata, Analysis of evaporation in the presence of composition-induced natural convection, *Int. J. Heat Mass Transfer* **28**, 1451–1459 (1985).
3. E. R. G. Eckert and R. M. Drake, *Heat and Mass Transfer*. McGraw-Hill, New York (1959).
4. R. B. Bird, W. E. Stewart and E. N. Lightfoot, *Transport Phenomena*. Wiley, New York (1960).
5. T. K. Sherwood, R. L. Pigford and C. R. Wilke, *Mass Transfer*. McGraw-Hill, New York (1975).
6. L. C. Burmeister, *Convective Heat Transfer*. Wiley, New York (1983).
7. J. M. Pommersheim and B. A. Ranck, Measurement of gaseous diffusion coefficients using the Stefan cell, *Ind. Engng Chem. Fundam.* **12**, 246–250 (1973).
8. C. Y. Lee and C. R. Wilke, Measurement of vapor diffusion coefficients, *Ind. Engng Chem.* **46**, 2381–2387 (1954).
9. A. T. Prata and E. M. Sparrow, Diffusion-driven nonisothermal evaporation, *J. Heat Transfer* **107**, 239–242 (1985).
10. S. V. Patankar, *Numerical Heat Transfer and Fluid Flow*. Hemisphere, Washington, D.C. (1980).
11. A. Settari and K. Aziz, A generalization of the additive-correction methods for the iterative solutions of matrix equations, *Siam J. Numer. Analysis* **10**, 506–521 (1973).
12. S. V. Patankar, A numerical method for conduction in composite materials, flow in irregular geometries, and conjugate heat transfer, *Proc. 6th Int. Heat Transfer Conf.* **3**, 297–302 (1978).
13. E. M. Sparrow and R. D. Cess, *Radiation Heat Transfer*. Hemisphere, Washington, D.C. (1978).

MODELES ET SOLUTIONS DE L'EVAPORATION ISOTHERME ET NON-ISOTHERME DANS UN TUBE PARTIELLEMENT REMPLI

Résumé—L'évaporation d'un bain liquide qui remplit partiellement un tube circulaire, dans une ambiance au repos, a été étudiée par plusieurs modèles accompagnés de résolutions numériques. La modélisation considère : (a) l'évaporation dans des conditions isothermes ou non à cause de l'absence ou de la présence d'un abaissement de température à la surface du liquide, (b) les interactions entre les champs de vitesse, de fraction de masse et de température pour la phase gaz–vapeur dans le tube et dans l'ambiance, (c) la convection naturelle dans l'espace gaz–vapeur, (d) le rayonnement dans l'espace gaz–vapeur, (e) la convection naturelle dans le bain liquide, et (f) la conduction dans l'enveloppe autour du tube, dans le tube et dans l'intervalle. En utilisant un système spécial de conditions de fermeture à l'extrémité supérieure du tube, on trouve que les flux d'évaporation (ou le nombre de Sherwood) peuvent être obtenus avec une précision acceptable sans avoir à étendre les résolutions numériques à l'ambiance. Une autre constatation est que l'abaissement de température à la surface du liquide diminue le nombre de Sherwood. Lorsque le transfert radiatif dans l'espace gaz–liquide est activé, l'abaissement de température décroit et le nombre de Sherwood augmente sensiblement. La convection naturelle dans le bain liquide agit aussi pour diminuer l'abaissement de température et pour augmenter le nombre de Sherwood.

ISOTHERME UND NICHTISOTHERME VERDUNSTUNG AUS EINEM TIELWEISE GEFÜLLTEN ROHR

Zusammenfassung—Die Verdunstung einer Flüssigkeit aus einem kreisrunden, teilweise gefüllten Rohr in eine ruhende Umgebung wurde mit Hilfe einer Reihe von Modellen untersucht. Die Modelle berücksichtigten : (a) Verdunstung unter isothermen als auch unter nichtisothermen Bedingungen, entsprechend dem Nichtvorhandensein oder dem Vorhandensein einer Temperaturabsenkung an der Flüssigkeitsoberfläche, (b) Wechselwirkungen zwischen den Geschwindigkeits-, Konzentrations- und Temperaturfeldern im Gas/Dampf-Raum im Rohr und in der Umgebung, (c) Natürliche Konvektion im Gas/Dampf-Raum, (d) Strahlungsaustausch im Gas/Dampf-Raum, (e) Natürliche Konvektion in der Flüssigkeit, (f) Wärmeleitung in der Wärmedämmung um das Rohr, in der Rohrwand und in der Schicht zwischen Rohr und Wärmedämmschicht. Mit Hilfe eines speziellen Satzes von Schließbedingungen am offenen Ende des Rohres konnten Verdunstungsraten (bzw. Sherwood-Zahlen) mit annehmbarer Genauigkeit berechnet werden, ohne die numerische Lösung auf die Umgebung erweitern zu müssen. Eine andere wichtige Erkenntnis war, daß die Temperaturabsenkung an der Flüssigkeitsoberfläche die Sherwood-Zahl verringert. Wurde der Strahlungsaustausch im Gas/Flüssigkeits-Raum berücksichtigt, so verringerte sich die Temperaturabsenkung und die Sherwood-Zahl wurde stark erhöht. Die natürliche Konvektion in der Flüssigkeit verringert ebenfalls die Temperaturabsenkung und erhöht die Sherwood-Zahl.

МОДЕЛИ И РЕШЕНИЯ ДЛЯ СЛУЧАЕВ ИЗОТЕРМИЧЕСКОГО И НЕИЗОТЕРМИЧЕСКОГО ИСПАРЕНИЯ ИЗ ТРУБЫ, ЧАСТИЧНО ЗАПОЛНЕННОЙ ЖИДКОСТЬЮ

Аннотация—На целом ряде моделей численно исследовано испарение из большого объема жидкости, которая частично заполняет круглую трубу, в неподвижную окружающую среду. Модели учитывали: (а) испарение как в изотермических, так и неизотермических условиях, когда имеет место или отсутствует понижение температуры поверхности жидкости, (б) взаимодействия между полями скорости, массосодержания и температуры в парогазовом пространстве в трубе и в окружающей среде, (в) естественная конвекция в парогазовом пространстве, (г) лучистый теплообмен в парогазовом пространстве, (д) естественная конвекция в объеме жидкости и (е) теплопроводность в изоляционном материале вокруг трубы, в ее стенке и в слое между трубой и изоляцией. Используя ряд специальных условий замыкания для открытой верхней части трубы, показано, что скорость испарения (т.е. число Шервуда) можно определить с приемлемой точностью, не решая уравнения переноса для окружающей среды. Кроме того, было установлено, что понижение температуры поверхности жидкости приводит к уменьшению числа Шервуда. В случае более интенсивного лучистого теплообмена в пространстве между газом и жидкостью температура снижалась меньше и число Шервуда возрастало. То же самое наблюдалось и при естественной конвекции в объеме жидкости.